

Adaptive model reduction of high-order solutions of compressible flows via optimal transport

R. Loek Van Heyningen^a, Ngoc Cuong Nguyen^a, Patrick Blonigan^b, Jaime Peraire^a

^aCenter for Computational Engineering, Department of Aeronautics and Astronautics, Massachusetts Institute of Technology, 77 Massachusetts Avenue, Cambridge, MA, 02139, USA

^bSandia National Laboratories, Livermore, 94450, CA, USA

Abstract

The solution of conservation laws with parametrized shock waves presents challenges for both high-order numerical methods and model reduction techniques. We introduce an r -adaptivity scheme based on optimal transport and apply it to develop reduced order models for compressible flows. The optimal transport theory allows us to compute high-order r -adaptive meshes from a starting reference mesh by solving the Monge–Ampère equation. A high-order discretization of the conservation laws enables high-order solutions to be computed on the resulting r -adaptive meshes. Furthermore, the Monge–Ampère solutions contain mappings that are used to reduce the spatial locality of the resulting solutions and make them more amenable to model reduction. We use a non-intrusive model reduction method to construct reduced order models of both the mesh and the solution. The procedure is demonstrated on three supersonic and hypersonic test cases, with the hybridizable discontinuous Galerkin method being used as the full order model.

Keywords: High-order methods, hybridizable discontinuous Galerkin methods, optimal transport, Monge–Ampère, model reduction, high-speed flow

1. Introduction

Numerical simulations of high-speed flow simulations have a key role to play in the development of supersonic and hypersonic technologies, for which the setup and monitoring of experiments can be costly and challenging. Many-query workflows such as design optimization or uncertainty quantification may require the repeated solution of partial differential equations (PDEs) with sharp features and shocks at different sets of operating parameters. When parametric uncertainty is considered for external hypersonic flow with strong shocks, it is often found that uncertainty in the free-stream Mach number has an outsized impact on the uncertainty in the quantities of interest, especially wall heat flux [24, 76, 68]. Therefore, it is essential that the solution of a parametric system of equations can accurately capture dynamics with moving shocks, and that any surrogate models used to make these workflows tractable can also handle parametric shock movement. Unfortunately, the parametric

variation of shocks poses challenges for classical numerical methods and model reduction techniques.

Low-order finite volume (FV) methods are still the most common choice for hypersonic simulations. However, it is well-known that for external flow problems with strong bow shocks, the quality of the computational mesh has a large impact on the solution when using most FV methods, with poorly designed but seemingly reasonable meshes resulting in non-physical results such as the carbuncle phenomenon [15, 50, 77]. Mesh adaptation can be used to avoid such issues, with automatic mesh refinement (AMR), anisotropically refined grids, and r -adaptive shock tracking methods having shown success for high-speed flow. Of particular note is the grid tailoring procedure of [71], which iteratively aligns grid lines with a strong bow shock and is implemented in state-of-the-art hypersonics codes such as US3D [16] and the Sandia Parallel Aerodynamics Reentry Code (SPARC) [35], among others. This procedure retains a fixed mesh topology and is thus an r -adaptive method.

An alternative to standard FV methods are high-order numerical methods, which have the potential to reach high levels of accuracy needed for high-fidelity simulations of complex phenomena. Discontinuous Galerkin (DG) methods are an attractive approach for CFD, due to their geometric flexibility, suitability for modern high-performance computer architectures, and amenability to adaptivity. Limiting the use of DG for high-speed flow is the fact that the presence of shocks can be particularly challenging for high-order methods, where the Gibbs phenomena can severely impact accuracy and robustness. The literature for shock capturing for DG methods is vast, with approaches including flux and slope limiting [12, 22, 43, 42, 48], locally low-order fluxes [38, 73, 66], and artificial viscosity (AV) methods [65, 64, 29, 5, 21, 1].

Manipulation of the computational mesh can also greatly improve resolution of sharp features when using high-order methods. Numerous works have coupled goal-oriented mesh adaptation with high-order methods for high-speed flow problems [5, 80, 51, 70, 1]. The relative benefits of r -adaptive shock-aligned meshes are arguably greater for high-order discontinuous methods; curved shocks can be tracked and high-order convergence is able to be regained when the shock alignment is performed exactly. By formulating the solution as an optimization problem over solution and mesh degrees of freedom, the High-Order Implicit Shock Tracking (HOIST) [82] and Moving DG with Interface Condition Enforcement (MDG-ICE) [23] methods can capture highly accurate solutions on coarse meshes. Both approaches have been applied to challenging hypersonic problems and returned accurate solutions on remarkably coarse meshes, including for viscous and reacting problems [20, 37, 81].

While accurate and robust evaluations of the full-order model (FOM) at different Mach numbers are important, so too is the development of accurate surrogate models. In parametric CFD, projection-based reduced order models (ROMs) have shown promise in delivering surrogate models that are efficient, can be coupled with rigorous error estimates, and exhibit low error even in high-dimensional parameter spaces and in regions of extrapolation. This context is where r -adaptivity can be especially impactful. If each snapshot of the FOM has a different grid topology, the definition of inner products between snapshots becomes non-trivial. Although some works [72, 47] have addressed this for AMR mesh adaptation, generalizing these approaches to anisotropically adapted meshes remains a challenge. A

more fundamental issue is that variation in the free-stream Mach number will usually cause shocks to move location; this means each FOM snapshot will have different locally coherent structures and the parametric solution manifold will suffer from a large Kolmogorov n -width. If the parametric variation is such that the shock does not move very much, classical linear model reduction techniques such as the proper orthogonal decomposition (POD) method can give acceptable answers [7]. As the variation increases, these methods will not be able to efficiently characterize the solution variation without a large amount of training data. Some degree of nonlinearity is usually required, such as with adaptively constructed or refined linear ROMs [17], a combination of FOM and ROM information in different parts of the domain [46, 36, 62, 83], or a choice of a nonlinear basis. Variations include linear bases augmented with nonlinear closure terms [2, 3], fully nonlinear bases [45, 41, 69], or bases that consist of combining a parameter-dependent mapping and a linear basis.

Examples of the latter for steady high-speed flow include the TSMOR method of [57], wherein mappings are derived based on wave speed arguments. The ROM-IFT [53] method minimizes over a reduced solution space and admissible domain mappings to align features, using similar arguments from the r -adaptive HOIST method. End-to-end efficiency gains are improved with greedy sampling of the solution and mapping space along with empirical quadrature-based hyperreduction [54]. The registration methods of [74] also compose a mapping and a linear basis. FOM snapshots are evaluated, a reference state is chosen, and a regularized optimal transport problem is solved to align the snapshots to some reference state. Recent improvements of the method include the incorporation of goal-oriented metric-based adaptation, empirical quadrature hyperreduction, and greedy multifidelity sampling methods [30, 4]. The grid-tailored ROMs of [19] use the outputs of a grid-tailored FV method simulation to construct a non-intrusive ROM for grid deformations and an intrusive ROM for the solution field.

Many of the aforementioned works emphasize the connection between r -adaptivity methods for the FOM and the learning of mappings that can be composed with a linear basis to form accurate ROMs for problems with moving features. In a similar vein, we make use of a recently developed high-order method for r -adaptivity based on optimal transport to aid in snapshot collection and data compression for model reduction of problems with parametrically varying shock structures. We propose that each FOM snapshot will include a solution field and mesh deformation. The mesh deformations are learned via solutions of the Monge-Ampère equation, an r -adaptation method derived from the application of optimal transport formulations to an equidistribution principal for mesh adaptation. Solutions of the Monge-Ampère equation have been used extensively for r -adaptivity [9, 11, 10, 52, 25, 67]. The equation can be challenging to solve with standard numerical methods, but the resulting meshes tend to avoid entanglements and smoothly transition between regions of refinement.

This is an elliptic equation that naturally handles curved boundaries and is itself amenable to model reduction [34].

A number of authors have used optimal transport ideas to remove or reduce the convective nature of parametrized problems [39, 14, 75, 6]. The most akin to ours are the registration methods of [74]. Registration methods form a regularized optimization statement of an optimal transport problem which explicitly maps snapshots onto a single reference

configuration. We solve the Monge-Ampère equation to map uniform mesh densities to relevant features; while we expect our method will do less to mitigate the Kolmogorov barrier than most optimal transport formulations since alignment is not explicitly targeted, it is a practical formulation that reuses our mesh adaptation procedure.

These mesh mappings can be applied to the FOM snapshots after training or they can be created as part of the FOM solution. We demonstrate the latter approach here. The mappings can be used as a mesh refinement strategy and an enabler for model reduction. This is similar to the examples of ROM-IFT coupled with HOIST, but is most similar to the grid-tailored ROMs of [19]. Grid tailoring is a shock alignment method while ours is not. Grid tailoring more explicitly aims for shocks to be fixed at a specific mesh degree of freedom. We sacrifice exact alignment for flexibility over grid tailoring, which is restricted to bow shocks and requires the ability to compute lines from the wall to the inflow boundary. The Monge-Ampère r -adaptivity can be used with structured and unstructured grids, tetrahedral or hexahedral elements, and can refine along various curved or interacting features, as long as they can be tracked by a scalar value monitor function.

The use of a high-order method for the flow solution allows for the PDE to be iteratively solved on anisotropically adapted meshes generated by the solution of the Monge-Ampère equation.

Some simplifications are made for this first study of the effectiveness of mappings constructed with Monge-Ampère mesh adaptation procedures in aiding model reduction. First, we only consider parametric variation in one parameter, the Mach number. This can still challenge linear basis ROMs, but the effects of the Kolmogorov barrier are in general less pronounced in this parameter regime and are more easily able to be overcome with sampling. Also, we only consider nonintrusive interpolation-based ROMs and test cases without extrapolation. With the small dimensional parameter spaces considered here, we expect nonintrusive interpolation ROMs to perform sufficiently well, while still providing insight into the effectiveness of this approach. It is worth mentioning that for steady high-speed flow problems, interpolation-based ROMs can be surprisingly effective for cases without extrapolation [7, 19].

The paper is organized as follows: Section 2 details the full order model discretization and proposed r -adaptivity scheme. The nonintrusive ROM formulations are presented in Section 3, while Section 4 shows results on three supersonic and hypersonic flow problems with varying degrees of shock strength and complexity. Conclusions and future work are described in Section 5.

2. Methods

2.1. Steady parametrized conservation laws

We consider a system of steady conservation laws on a domain $\Omega \in \mathbb{R}^d$

$$\nabla \cdot \mathbf{F}(\mathbf{u}(\mathbf{x}; \boldsymbol{\mu}); \boldsymbol{\mu}) = 0, \quad \forall \mathbf{x} \in \Omega \quad (1)$$

where $\mathbf{u} \in \mathbb{R}^m$ is the solution with m components, $\boldsymbol{\mu} \in \mathcal{D} \subset \mathbb{R}^q$ is a vector of parameters, and $\mathbf{F} \in \mathbb{R}^{m \times d}$ is a physical flux function. The domain Ω is partitioned into a collection

of disjoint elements \mathcal{T}_h and parametrically varying boundary conditions are specified on the boundary $\Gamma \in \partial\Omega$.

For this work, we exclusively solve the compressible Euler equations in conservative form,

$$\mathbf{u} = \begin{pmatrix} \rho \\ \rho v_i \\ \rho E \end{pmatrix}, \quad \mathbf{F}_i = \begin{pmatrix} \rho v_i \\ \rho v_i v_j + \delta_{ij} p \\ \rho v_i H \end{pmatrix} \quad (2)$$

with density ρ , velocity \mathbf{v} , total energy E , total specific enthalpy $H = E + p/\rho$ and pressure p given by the ideal gas law. Let $\Gamma_{\text{wall}} \subset \partial\Omega$ be the wall boundary. The boundary condition at the wall boundary Γ_{wall} is $\mathbf{v} \cdot \mathbf{n} = 0$, where \mathbf{v} is the velocity field and \mathbf{n} is the unit normal vector outward the boundary. Because supersonic and hypersonic flows are considered in this paper, supersonic inflow and outflow conditions are imposed on the inflow and outflow boundaries, respectively.

2.2. Adaptive viscosity regularization

For discretizing and solving (1), we use the adaptive viscosity regularization approach of [61]. For clarity, we drop the parametric dependence for this section. While not the focus of this work, we give a brief overview for context, as this method allows for the rapid and reliable solution of the shock-dominated examples below. Instead of solving (1) directly, we augment it with an artificial viscosity regularization term \mathbf{G} and an equation to smooth out the resulting artificial viscosity, in line with PDE-based artificial viscosity approaches [5]

$$\nabla \cdot \mathbf{F}(\mathbf{u}) - \lambda_1 \nabla \cdot \mathbf{G}(\mathbf{u}, \nabla \mathbf{u}, \eta) = 0 \quad \text{in } \Omega, \quad (3a)$$

$$\eta - \lambda_2^2 \nabla \cdot (\ell^2 \nabla \eta) - s(\mathbf{u}, \nabla \mathbf{u}) = 0 \quad \text{in } \Omega \quad (3b)$$

where the Helmholtz equation in (3b) is assigned homogeneous boundary conditions $\eta = 0$ at the wall boundary and $\nabla \eta \cdot \mathbf{n} = 0$ at the remaining boundary. The term $s(\mathbf{u}, \nabla \mathbf{u})$ is defined as

$$s(\mathbf{u}, \nabla \mathbf{u}) = g_{\text{clip}}(\mathcal{S}(\mathbf{u}, \nabla \mathbf{u}); s_{\text{min}}, s_{\text{max}}) \quad (4)$$

where $g_{\text{clip}}(\cdot; s_{\text{min}}, s_{\text{max}})$ is a smooth function that limits the first argument between s_{min} and s_{max} . The term $\mathcal{S}(\mathbf{u}, \nabla \mathbf{u})$ is a shock sensor, here chosen to be the negative divergence of the velocity [56]

$$\mathcal{S}(\mathbf{u}, \nabla \mathbf{u}) = -\nabla \cdot \mathbf{v}. \quad (5)$$

The limiting parameters are chosen as in [61], with $s_{\text{min}} = 0$ to avoid negative viscosity and s_{max} is set iteratively to $0.5 \|\mathcal{S}\|_{\infty}$. Artificial dissipation is added with $\mathbf{G}(\mathbf{u}, \nabla \mathbf{u})$, defined as

$$\mathbf{G}(\mathbf{u}, \nabla \mathbf{u}, \eta) = \mu(\eta) \nabla \mathbf{u}. \quad (6)$$

The parameters λ_1, λ_2 which control the magnitude and width of the artificial viscosity respectively, are iteratively ramped down until regularity or physical constraints are violated. In other words, the method aims to minimize the amount of artificial viscosity while maintaining smooth and accurate solutions. The method acts as a nonlinear solver and procedure for controlling artificial viscosity amounts [61].

Equation (3a) is discretized with a hybridized discontinuous Galerkin (HDG) method while (3b) is discretized with continuous Galerkin (CG). HDG is chosen for the flow system due to its stability for convective problems and reduced globally coupled degrees of freedom compared to standard DG methods. See [58, 59, 27, 55, 63, 78, 31, 28] for more details on the HDG discretization of the Euler equations, including the precise weak form statements, static condensation solution procedures, and boundary conditions. CG is used for the Helmholtz equation (3b) so that the artificial viscosity field is continuous, which tends to result in more robust artificial viscosity methods [1, 21, 5].

As emphasized in [61], the amount of artificial viscosity depends on the mesh. In the extreme case of perfect alignment of shocks with element faces for discontinuous schemes with a suitable numerical Riemann solver, no viscosity is needed [23, 82]. In [61], a solution on an initial mesh was used to locate shock structures and a new shock-aligned mesh was generated. While capable of producing high-quality solutions, when solving parametric systems of PDEs, this procedure would generate meshes with different topologies for each snapshot.

2.3. Mesh adaptation

2.3.1. Monge-Ampère equation for mesh adaptation

Mesh adaptation is accomplished via high-order solutions of the Monge-Ampère equation of optimal transport, based on the method introduced in [60]. Mesh adaptation using the Monge-Ampère is usually oriented around an equidistribution principle. Suppose we are given a target $\boldsymbol{\mu}$ -dependent density function $\rho'(\boldsymbol{x}; \boldsymbol{\mu})$ and a source $\boldsymbol{\mu}$ -dependent density function $\rho(\boldsymbol{x}; \boldsymbol{\mu})$ defined on Ω . The optimal transport problem seeks to find a mapping $\phi(\boldsymbol{x})$ such that

$$\inf_{\phi \in \mathcal{M}_\mu} \int_{\Omega} \|\boldsymbol{x} - \phi(\boldsymbol{x}; \boldsymbol{\mu})\|^2 \rho(\boldsymbol{x}; \boldsymbol{\mu}) d\boldsymbol{x} \quad (7)$$

with

$$\mathcal{M}_\mu = \{\phi : \Omega \rightarrow \Omega, \rho'(\phi(\boldsymbol{x}; \boldsymbol{\mu}); \boldsymbol{\mu}) \det(\nabla \phi(\boldsymbol{x}; \boldsymbol{\mu})) = \rho(\boldsymbol{x}; \boldsymbol{\mu}), \forall \boldsymbol{x} \in \Omega\} \quad (8)$$

being defined as the set of feasible mappings. Under certain regularity conditions described by Brenier [8] and Caffarelli [13], the optimal map of (7) is equal to the gradient of a scalar convex potential w . Inserting $\phi(\boldsymbol{x}; \boldsymbol{\mu}) = \nabla w(\boldsymbol{x}; \boldsymbol{\mu})$ into the feasible set of \mathcal{M}_μ gives the parametrized Monge-Ampère equation

$$\rho'(\nabla w(\boldsymbol{x}; \boldsymbol{\mu}); \boldsymbol{\mu}) \det(D^2 w(\boldsymbol{x}; \boldsymbol{\mu})) = \rho(\boldsymbol{x}; \boldsymbol{\mu}). \quad (9)$$

We require that that ϕ conforms to the physical boundary $\partial\Omega$. If the physical boundary $\partial\Omega$ can be expressed as the equation $g(\boldsymbol{x}) = 0$ for $\boldsymbol{x} \in \partial\Omega$, we impose the following nonlinear Neumann boundary condition:

$$g(\nabla w(\boldsymbol{x}; \boldsymbol{\mu})) = 0, \forall \boldsymbol{x} \in \partial\Omega. \quad (10)$$

Mesh adaptation by the equidistribution principle means that the source density is a uniform redistribution of the target density on the domain. Therefore, we have $\rho(\boldsymbol{x}; \boldsymbol{\mu}) = \theta(\boldsymbol{\mu})$ for

$\theta(\boldsymbol{\mu}) = \int_{\Omega} \rho'(\boldsymbol{x}; \boldsymbol{\mu}) d\boldsymbol{x} / \int_{\Omega} d\boldsymbol{x}$. The Monge-Ampère equation can then be written as

$$\det(D^2 w(\boldsymbol{x}; \boldsymbol{\mu})) = f(\nabla w(\boldsymbol{x}; \boldsymbol{\mu}); \boldsymbol{\mu}), \quad \forall \boldsymbol{x} \in \Omega, \quad (11a)$$

$$g(\nabla w(\boldsymbol{x}; \boldsymbol{\mu})) = 0, \quad \forall \boldsymbol{x} \in \partial\Omega, \quad (11b)$$

$$\int_{\Omega} w(\boldsymbol{x}; \boldsymbol{\mu}) d\boldsymbol{x} = 0, \quad (11c)$$

where $f(\nabla w(\boldsymbol{x}; \boldsymbol{\mu}); \boldsymbol{\mu}) = \theta(\boldsymbol{\mu}) / \rho'(\nabla w(\boldsymbol{x}; \boldsymbol{\mu}); \boldsymbol{\mu})$. The Monge-Ampère equation (11) is a nonlinear elliptic PDE with a nonlinear Neumann boundary condition.

For two dimensions, the Monge-Ampère equation can also be written as

$$\boldsymbol{H} - \nabla \boldsymbol{q} = 0, \quad \text{in } \Omega \quad (12a)$$

$$\boldsymbol{q} - \nabla w = 0, \quad \text{in } \Omega \quad (12b)$$

$$S(\boldsymbol{H}, \boldsymbol{q}; \boldsymbol{\mu}) - \nabla \cdot \boldsymbol{q} = 0, \quad \text{in } \Omega \quad (12c)$$

$$g(\boldsymbol{q}) = 0, \quad \text{on } \partial\Omega \quad (12d)$$

$$\int_{\Omega} w(\boldsymbol{x}) d\boldsymbol{x} = 0 \quad (12e)$$

with $S(\boldsymbol{H}, \boldsymbol{q}; \boldsymbol{\mu}) = \sqrt{H_{11}^2 + H_{22}^2 + H_{12}^2 + H_{21}^2 + 2f(\boldsymbol{q}; \boldsymbol{\mu})}$. Equation 12 is discretized in space with an HDG method described in [60]. The static condensation procedure of HDG means that the size of the global unknowns scales with the trace of the scalar variable, not of the gradient or Hessian terms. For smooth analytic choices of target density, it was found that the solution, gradient, and Hessian all converge with the same order of accuracy. Finally, the use of HDG allows for solutions on unstructured grids and curved boundaries, meaning that the starting reference mesh can be high-order and unstructured.

In the remainder of the paper, the subscript h will indicate the numerical solution computed by using the HDG method. Hence, the mapping \boldsymbol{q}_h is an approximation to the exact mapping $\boldsymbol{\phi}(\boldsymbol{x})$, which is a discontinuous field. It means that a single vertex will have two separate mappings that are not required to be equal. In practice, we use a continuous approximation of \boldsymbol{q}_h by averaging the duplicate degrees of freedom of \boldsymbol{q}_h , which shall be denoted as $\boldsymbol{\phi}_h$. A more subtle issue is the presence of corners inside the domain. Other r -adaptivity procedures have found it useful to constrain corner nodes [32, 37]. Since the mesh mapping is given by the *gradient* of a scalar potential, it is not obvious how to constrain corner nodes. It was found that geometries with internal corners posed challenges for the HDG Monge-Ampère solver. This can be avoided by making sure that $g(\cdot) = 0$ is a *global* description of the geometry. For example, suppose we have a boundary with intersecting lines $g_1(\boldsymbol{x}) = 0$ for $\boldsymbol{x} \in \Gamma_1$ and $g_2(\boldsymbol{x}) = 0$ for $\boldsymbol{x} \in \Gamma_2$. When evaluating (12d) on a face that lies on Γ_1 , rather than always letting $g_1(\nabla u_h) = 0$, we switch to enforcing $g_2(\nabla u_h) = 0$ if $\nabla u_h \in \Gamma_2$. This approach, though allowing the solver to converge, lets boundary nodes transition from one boundary to another. This means corner nodes can get detached from corners, which can be manually corrected in the mapping. It also means that nodes that were once a wall boundary can move to an outflow boundary, for example. For our solver, this just means that the mapped mesh needs to be reinitialized and reassigned boundary conditions.

2.3.2. Adaptation Procedure

We still need to define the mesh density function $\rho'(\mathbf{x}; \boldsymbol{\mu})$ in order to obtain a good r -adaptive mesh $\phi_h(\mathbf{x}; \boldsymbol{\mu})$. The optimal transport will drive mesh nodes to concentrate around high values of the mesh density function. Therefore, $\rho'(\mathbf{x}; \boldsymbol{\mu})$ should be large in the region where refinement is needed and small elsewhere. It is possible to choose the artificial viscosity field as a target density so that the r -adaptive mesh $\phi_h(\mathbf{x}; \boldsymbol{\mu})$ is fine in the shock region. However, the dilatation sensor used can fail to detect other sharp features including contact discontinuities. Instead, we use the gradient of a scalar function $\xi_h(\mathbf{x}; \boldsymbol{\mu})$ to define a resolution sensor:

$$s_h(\mathbf{x}; \boldsymbol{\mu}) = \sqrt{1 + g_{\text{clip}}(\|\nabla \xi_h(\mathbf{x}; \boldsymbol{\mu})\|_{\Omega}^2; s_{\min}, s_{\max})} \quad (13)$$

where $s_{\min} = 0$ and $s_{\max} = 0.5\|\nabla \xi_h(\mathbf{x}; \boldsymbol{\mu})\|_{\infty}$. The mesh density function is computed by solving the following Helmholtz equation

$$\rho'(\mathbf{x}; \boldsymbol{\mu}) - \nabla \cdot (\ell^2 \nabla \rho'(\mathbf{x}; \boldsymbol{\mu})) = s_h(\mathbf{x}; \boldsymbol{\mu}) \quad \text{in } \Omega, \quad (14)$$

with homogeneous Neumann boundary conditions on the whole domain. This is a feature-based adaptation indicator. Other indicators are possible, such as those based on adjoint information or some combination of physics-based artificial viscosity sensors that can distinguish between shocks, large temperature gradients, and other sharp features. The only requirement is that an indicator function be expressed as a scalar-valued positive function.

It remains to describe how to choose the scalar function $\xi_h(\mathbf{x}; \boldsymbol{\mu})$. In this paper, we choose $\xi_h(\mathbf{x}; \boldsymbol{\mu})$ as the approximate fluid density obtained by using the adaptive viscosity regularization method described in Subsection 2.2. More specifically, let \mathcal{T}_h^0 denote the high-order reference mesh on the physical domain Ω . Note that the reference mesh \mathcal{T}_h^0 is independent of $\boldsymbol{\mu}$. For any given $\boldsymbol{\mu} \in \mathcal{D}$, we repeatedly solve the system (3) and reduce the values of λ_1, λ_2 by using the HDG/CG scheme with the reference mesh \mathcal{T}_h^0 until any of the smoothness and positivity constraints is violated. This yields $\mathbf{u}_h^0(\mathbf{x}; \boldsymbol{\mu})$ as the numerical approximation to the exact solution \mathbf{u} of the conservation laws (1). Then $\xi_h(\mathbf{x}; \boldsymbol{\mu})$ is nothing but the first component of $\mathbf{u}_h^0(\mathbf{x}; \boldsymbol{\mu})$.

The fact that the target mesh density ρ' is the solution of the Helmholtz equation (14) makes the Monge-Ampère equation more expensive to be solved numerically. Specifically, the fixed point scheme is used to solve the Monge-Ampère equation (12). At the l -th iteration of the fixed point scheme, we evaluate $S(\mathbf{H}_h^{l-1}, \mathbf{q}_h^{l-1}; \boldsymbol{\mu})$ which in turn requires us to evaluate $\rho'(\mathbf{q}_h^{l-1}; \boldsymbol{\mu})$. Because the mesh density function ρ' is constructed from local polynomials of high degree on the reference mesh \mathcal{T}_h^0 , we must interpolate it onto $\mathbf{q}_h^{l-1}(\boldsymbol{\mu})$. The interpolation of a scalar field from one high-order mesh to another high-order mesh can be computationally expensive. The fixed-point scheme reaches a convergence when $\|\mathbf{q}_h^l(\boldsymbol{\mu}) - \mathbf{q}_h^{l-1}(\boldsymbol{\mu})\|_{\Omega}$ is less than a specified tolerance. At convergence, $\mathbf{q}_h^l(\boldsymbol{\mu})$ is averaged at the duplicate degrees of freedom to yield the mapping $\phi_h(\boldsymbol{\mu})$, which defines the resulting r -adaptive mesh $\mathcal{T}_h^{\boldsymbol{\mu}}$. The mesh adaptation procedure is described in Algorithm 1.

To clarify each step of Algorithm 1, we consider a sample flow field with a single bow shock in front of a cylindrical body. Representative inputs and outputs are shown in Figure 1 for a free-stream Mach number of $\boldsymbol{\mu} = 2.0$.

Algorithm 1 Monge-Ampère mesh adaptation for steady parametrized problems.

Input: The reference mesh \mathcal{T}_h^0 and parameters $\boldsymbol{\mu} \in \mathcal{D}$.

Output: The mapping $\phi_h(\boldsymbol{\mu})$ that maps the reference mesh \mathcal{T}_h^0 to the adaptive mesh \mathcal{T}_h^μ , and the numerical solution $\mathbf{u}_h(\boldsymbol{\mu})$ on \mathcal{T}_h^μ .

- 1: Solve for $\mathbf{u}_h^0(\boldsymbol{\mu})$ on \mathcal{T}_h^0 using the adaptive viscosity regularization method.
 - 2: Compute the target mesh density $\rho'(\mathbf{x}; \boldsymbol{\mu})$ based on \mathbf{u}_h^0 by using (13) and (14).
 - 3: Solve the Monge-Ampère equation (12) on \mathcal{T}_h^0 using the fixed-point HDG method.
 - 4: Average \mathbf{q}_h to obtain the mapping $\phi_h(\boldsymbol{\mu})$ and the associated r -adaptive mesh \mathcal{T}_h^μ .
 - 5: Interpolate $\mathbf{u}_h^0(\boldsymbol{\mu})$ onto \mathcal{T}_h^μ and use it as the initial guess.
 - 6: Solve for $\mathbf{u}_h(\boldsymbol{\mu})$ on \mathcal{T}_h^μ using the adaptive viscosity regularization method.
-

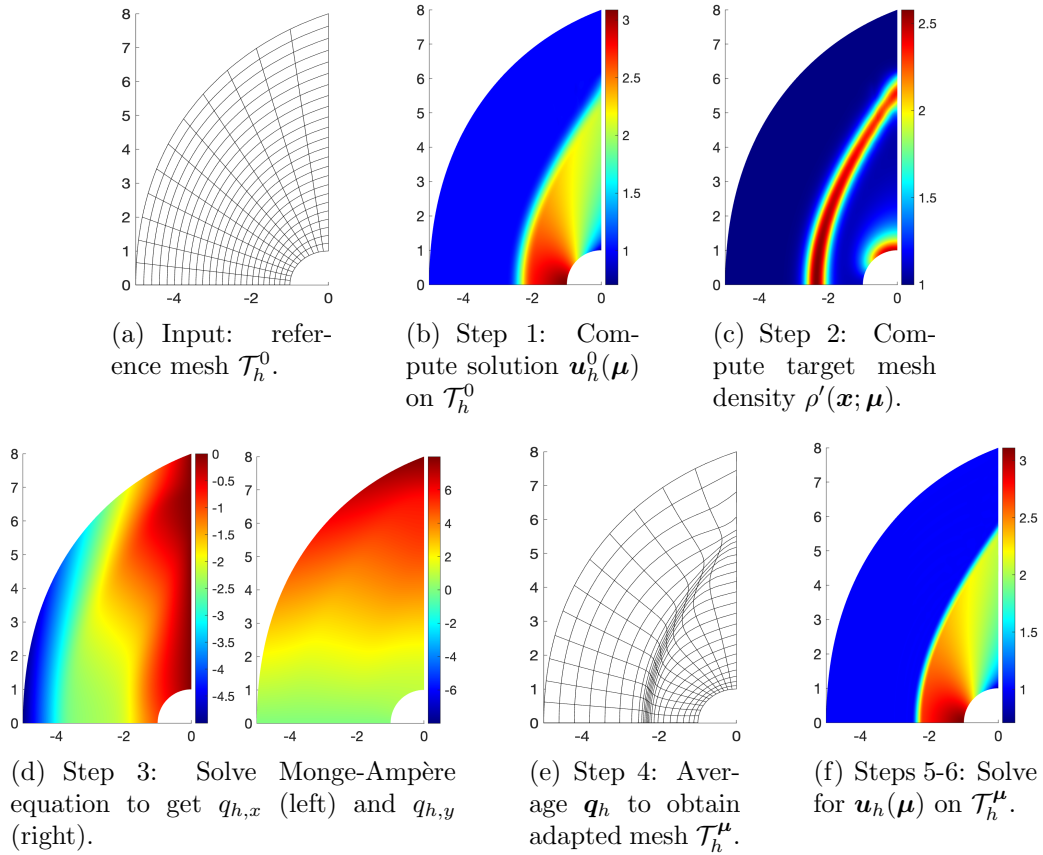


Figure 1: Visualization of steps of Algorithm 1.

3. Reduced Order Modeling

3.1. Model reduction on the reference domain

In addition to allowing for mesh adaptation to be performed during the training of a reduced-order model, the optimal transport method also makes it convenient to map the

numerical solution $u_h(\mathbf{x}; \boldsymbol{\mu}_i)$ from the r -adaptive mesh \mathcal{T}_h^μ to the reference domain \mathcal{T}_h^0 . In r -adaptivity, mesh points are neither created nor destroyed, connectivity structure does not need to be modified. We exploit this property of r -adaptivity to construct reduced order models.

We perform Algorithm 1 for a given set of training parameters $\{\boldsymbol{\mu}_i\}_{i=1}^{n_{\text{train}}}$ to obtain snapshots of the numerical solution $\{\mathbf{u}_h(\mathbf{x}; \boldsymbol{\mu}_i)\}_{i=1}^{n_{\text{train}}}$ and the mapping, $\{\phi_h(\mathbf{x}; \boldsymbol{\mu}_i)\}_{i=1}^{n_{\text{train}}}$. Note that all of the mapping snapshots $\{\phi_h(\mathbf{x}; \boldsymbol{\mu}_i)\}_{i=1}^{n_{\text{train}}}$ are defined on the reference mesh \mathcal{T}_h^0 , whereas the solution snapshots $\{\mathbf{u}_h(\mathbf{x}; \boldsymbol{\mu}_i)\}_{i=1}^{n_{\text{train}}}$ are defined on different $\boldsymbol{\mu}$ -dependent adaptive meshes $\mathcal{T}_h^{\mu_i}$. If \mathbf{x} is mesh point in \mathcal{T}_h^0 then $\phi_h(\mathbf{x}; \boldsymbol{\mu}_i)$ is a mesh point in $\mathcal{T}_h^{\mu_i}$. We then introduce

$$\tilde{\mathbf{u}}_h(\mathbf{x}; \boldsymbol{\mu}_i) = \mathbf{u}_h(\phi(\mathbf{x}; \boldsymbol{\mu}_i); \boldsymbol{\mu}_i), \quad \forall \mathbf{x} \in \mathcal{T}_h^0. \quad (15)$$

The resulting snapshots $\{\tilde{\mathbf{u}}_h(\mathbf{x}; \boldsymbol{\mu}_i)\}_{i=1}^{n_{\text{train}}}$ are defined on the reference mesh \mathcal{T}_h^0 . On the reference mesh, we anticipate that sharp features will be smoothed out and brought into closer alignment, making model reduction more effective. Model reduction can then be performed on the snapshots of ϕ_h , which are anticipated to be smooth due to the elliptic nature of the Monge-Ampère equation, and the snapshots of $\tilde{\mathbf{u}}_h$, which are anticipated to be more regular than \mathbf{u}_h and with less parametric variation.

The quantities used to construct these ROMs are shown in Figure 2 using the same high-speed cylinder flow introduced in Subsection 2.3.2 with a training set of $\mathcal{D} = \{2, 3, 4\}$.

3.2. Interpolation ROMs

We construct nonintrusive interpolation-based ROMs for the mapping and the solution both defined on the reference mesh.

For simplicity, we consider external supersonic and hypersonic configurations with one parameter allowed to vary, the free stream Mach number $\boldsymbol{\mu} = \text{Ma}_\infty$, and with the training set fixed for each problem.

We compress the snapshots of the solution and mapping with the proper orthogonal decomposition approach. Snapshots of $\tilde{\mathbf{u}}_h$ and ϕ_h are arranged into matrices $\mathbf{X}_{\tilde{\mathbf{u}}}$ and \mathbf{X}_ϕ respectively. The SVD is taken of each matrix to extract the leading modes

$$\mathbf{U}_{\tilde{\mathbf{u}}}\boldsymbol{\Sigma}_{\tilde{\mathbf{u}}}\mathbf{V}_{\tilde{\mathbf{u}}}^T = \mathbf{X}_{\tilde{\mathbf{u}}}, \quad \mathbf{U}_\phi\boldsymbol{\Sigma}_\phi\mathbf{V}_\phi^T = \mathbf{X}_\phi, \quad (16)$$

and the reduced bases for the solution and maps $\mathbf{W}_{\tilde{\mathbf{u}}}$ and \mathbf{W}_ϕ are defined as the N leading columns of \mathbf{U} , where $N \leq n_{\text{train}}$ is the reduced basis dimension.

For any given $\boldsymbol{\mu} \in \mathcal{D}$, the best approximations of the solution and the mapping are given by

$$\tilde{\mathbf{u}}_N^*(\boldsymbol{\mu}) = \mathbf{W}_{\tilde{\mathbf{u}}}\boldsymbol{\alpha}_{\tilde{\mathbf{u}}}^*(\boldsymbol{\mu}), \quad \phi_N^*(\boldsymbol{\mu}) = \mathbf{W}_\phi\boldsymbol{\alpha}_\phi^*(\boldsymbol{\mu}), \quad (17)$$

where the $\boldsymbol{\alpha}^*$ vectors are the coefficients of the best approximations and are given by

$$\boldsymbol{\alpha}_{\tilde{\mathbf{u}}}^*(\boldsymbol{\mu}) = \mathbf{W}_{\tilde{\mathbf{u}}}^T\tilde{\mathbf{u}}_h(\boldsymbol{\mu}), \quad \boldsymbol{\alpha}_\phi^*(\boldsymbol{\mu}) = \mathbf{W}_\phi^T\phi_h(\boldsymbol{\mu}). \quad (18)$$

Because the coefficients of the best approximations require the solution and the mapping, they can be only computed for $\boldsymbol{\mu} = \boldsymbol{\mu}_i, 1 \leq i \leq n_{\text{train}}$, in the training set. As a result, the best approximations are for those parameter vectors in the training set.

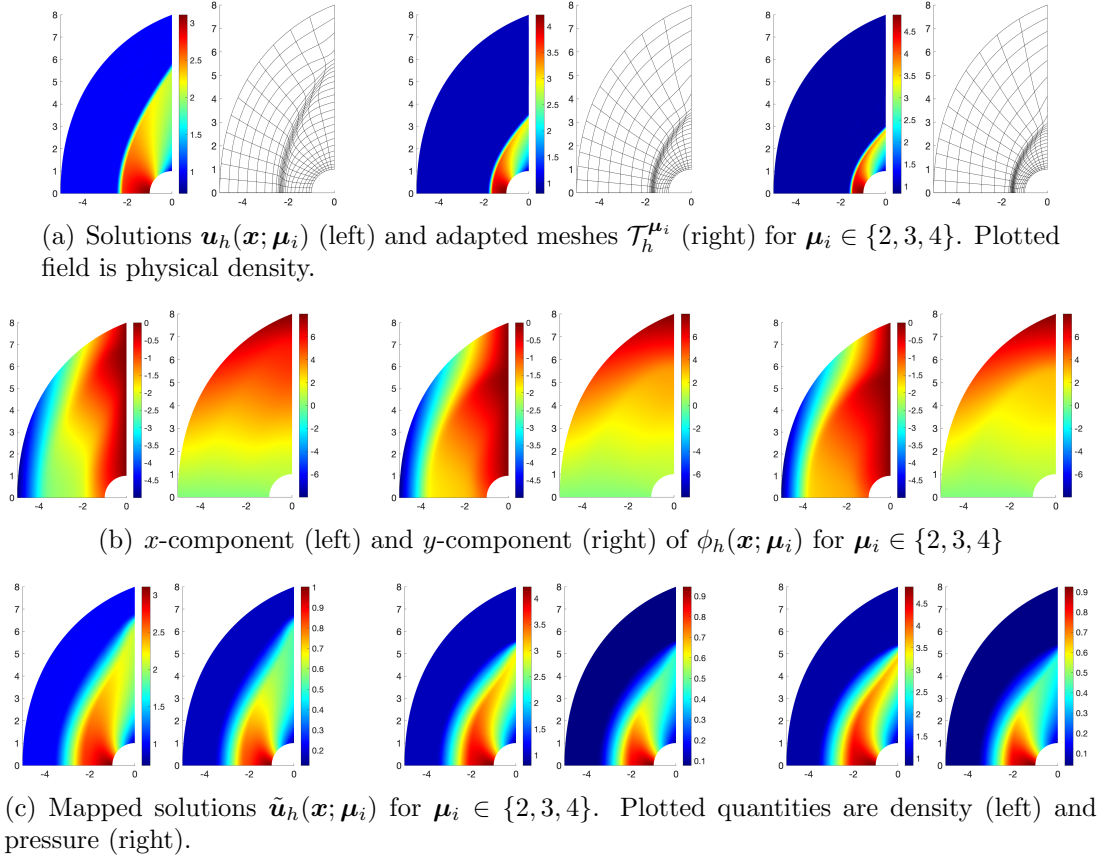


Figure 2: Sample quantities used to build ROM for different parameter samples. Top row contains the outputs of Algorithm 1, solutions $\{\mathbf{u}_h(\mathbf{x}; \boldsymbol{\mu}_i)\}_{i=1}^3$ and adapted meshes $\{\mathcal{T}_h^{\boldsymbol{\mu}_i}\}_{i=1}^3$. Middle row shows the corresponding mappings $\{\phi_h(\mathbf{x}; \boldsymbol{\mu}_i)\}_{i=1}^3$ for each adapted mesh. Bottom row displays solutions mapped back to the reference domain, $\{\tilde{\mathbf{u}}_h(\mathbf{x}; \boldsymbol{\mu}_i)\}_{i=1}^3$.

For any $\boldsymbol{\mu} \in \mathcal{D}$ which does not reside in the training set, we compute the ROM approximations of the solution and mapping as follows

$$\tilde{\mathbf{u}}_N(\boldsymbol{\mu}) = \mathbf{W}_{\tilde{\mathbf{u}}} \boldsymbol{\alpha}_{\tilde{\mathbf{u}}}(\boldsymbol{\mu}), \quad \phi_N(\boldsymbol{\mu}) = \mathbf{W}_{\phi} \boldsymbol{\alpha}_{\phi}(\boldsymbol{\mu}). \quad (19)$$

The $\boldsymbol{\alpha}$ vectors are the coefficients of the solution expanded in the reduced basis \mathbf{W} and are referred to as the generalized coordinates.

We use the simple radial basis function (RBF) surrogate used as an initial guess for an intrusive ROM in [19]. More sophisticated RBF ROMs are possible, usually involving some calibration with a mix of training and testing sets [26, 79, 33].

The RBF interpolant is defined as

$$\alpha_n(\boldsymbol{\mu}) = \sum_{i=1}^{n_{\text{train}}} \beta_{ni} \Psi(\|\boldsymbol{\mu} - \boldsymbol{\mu}_i\|_2), \quad 1 \leq n \leq N, \quad (20)$$

where Ψ are radial basis functions. For this work, we use a multiquadratic radial basis function with shape parameter set to 20. The coefficients β_{ni} are determined by enforcing that $\boldsymbol{\alpha}(\boldsymbol{\mu}_i)$ are equal to $\boldsymbol{\alpha}^*(\boldsymbol{\mu}_i)$ for all $\boldsymbol{\mu}_i$ in the training set and solving a $n_{\text{train}} \times n_{\text{train}}$ linear system. In [19], the resulting interpolant was found to be reasonably competitive with an intrusive ROM when interpolating in parameter space, considering the relative ease of training and online evaluations.

4. Numerical examples

For each case we compare a *mapped ROM* to a *fixed mesh ROM*. The mapped ROM uses the quantities described in Subsection 3.1, the mappings $\{\phi_h(\mathbf{x}; \boldsymbol{\mu}_i)\}_{i=1}^{n_{\text{train}}}$ and mapped snapshots $\{\tilde{\mathbf{u}}_h(\mathbf{x}; \boldsymbol{\mu}_i)\}_{i=1}^{n_{\text{train}}}$. The fixed mesh ROM builds a ROM using snapshots of $\{\mathbf{u}_h^0(\mathbf{x}; \boldsymbol{\mu}_i)\}_{i=1}^{n_{\text{train}}}$, from step 1 of Algorithm 1. We use a reasonable starting mesh for each case so that the snapshots of \mathbf{u}_h^0 are of acceptable quality.

We report the relative ℓ^2 errors of a vector field $\mathbf{v}_h(\mathbf{x}; \boldsymbol{\mu})$. For the mixed mesh ROM, \mathbf{v}_h is $\mathbf{u}^0(\mathbf{x}; \boldsymbol{\mu})$. For the mapped mesh ROMs there are two fields to consider, $\phi_h(\mathbf{x}; \boldsymbol{\mu})$ and $\tilde{\mathbf{u}}_h(\mathbf{x}; \boldsymbol{\mu})$. The ℓ^2 error over a test set $\mathcal{S}_{\text{test}} \in \mathcal{D}$ on the reference domain Ω is given by

$$E_v(\boldsymbol{\mu}) = \sqrt{\frac{\int_{\Omega} \|\mathbf{v}_h(\mathbf{x}; \boldsymbol{\mu}) - \mathbf{W}_v \boldsymbol{\alpha}_v(\boldsymbol{\mu})\|_2^2}{\int_{\Omega} \|\mathbf{v}(\mathbf{x}; \boldsymbol{\mu})\|_2^2}}, \quad \forall \boldsymbol{\mu} \in \mathcal{S}_{\text{test}}. \quad (21)$$

Errors are computed on the reference mesh due to the fact that there may be non-negligible error in the mappings, so a reference solution at any test parameter will have a slightly different grid than the ROM. Furthermore, the errors on the reference mesh will more clearly show whether the solution $\tilde{\mathbf{u}}_h$ is indeed more amenable to model reduction on the reference domain for practical mesh mappings. For examples with a wide range of Mach numbers, we evaluate at test sets that are equally spaced in between the training sets in order to account for the full variation of flow conditions. In all cases, the mean and max errors over the test set are reported.

4.1. Flow around a cylinder

We consider inviscid flow around a cylinder geometry with parametrically varying Mach number. These configurations are a common benchmark for shock capturing methods for high-speed flow [29, 21, 44, 1]. The flow exhibits a strong curved bow shock that varies parametrically with the Mach number. The free-stream Mach number is varied between supersonic and hypersonic ranges, with $\mathcal{D} = [2, 10]$.

For each FOM solution, we begin with a reference mesh with 25 elements in the radial and axial directions, with polynomial order 3. The reference mesh is shown in Figure 3. Each FOM is solved from a uniform solution initialized to the free-stream values with no polynomial order continuation.

The solutions $\mathbf{u}_h(\mathbf{x}; \boldsymbol{\mu})$, adapted meshes \mathcal{T}_h^μ , and mapped solutions $\tilde{\mathbf{u}}_h(\mathbf{x}; \boldsymbol{\mu})$ for representative values choices of $\boldsymbol{\mu}$ are shown in Figure 4.

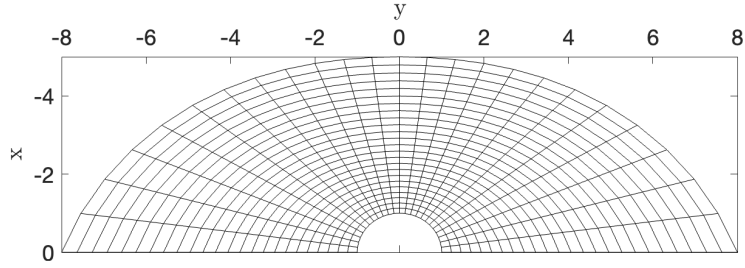
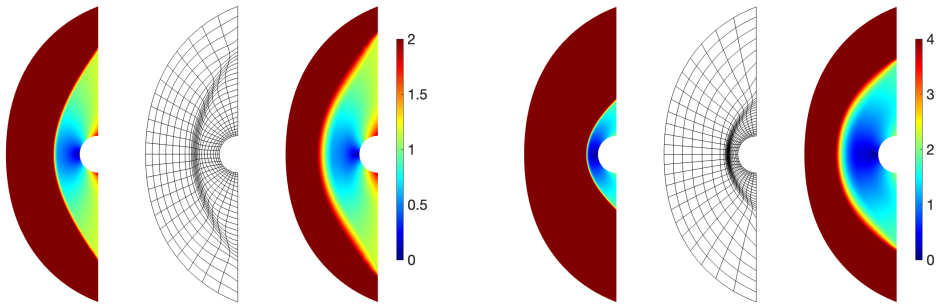
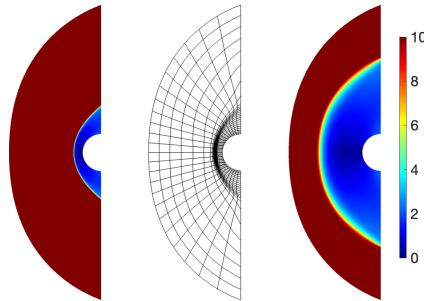


Figure 3: Starting structured grid of Ω for the high-speed cylinder.



(a) $\text{Ma}_\infty = 2.0$

(b) $\text{Ma}_\infty = 4.0$



(c) $\text{Ma}_\infty = 10.0$

Figure 4: For different Mach numbers, a visualization of the solution $\mathbf{u}_h(\mathbf{x})$, the corresponding adapted mesh \mathcal{T}_h^μ and the solution mapped back to the reference domain $\hat{\mathbf{u}}_h$. Plotted quantity is the Mach number.

Although the snapshots of $\tilde{\mathbf{u}}_h$ are not perfectly aligned, the parametric shock motion is substantially reduced.

Most of the shock movement occurs towards the outflow boundaries; along the stagnation line, the shock is brought into near alignment. See Figure 5. For shocks that are stabilized with some artificial viscosity, reversing the mapping also has the effect of smearing out sharp

features. The combination of alignment and smearing should abet classical model reduction procedures.

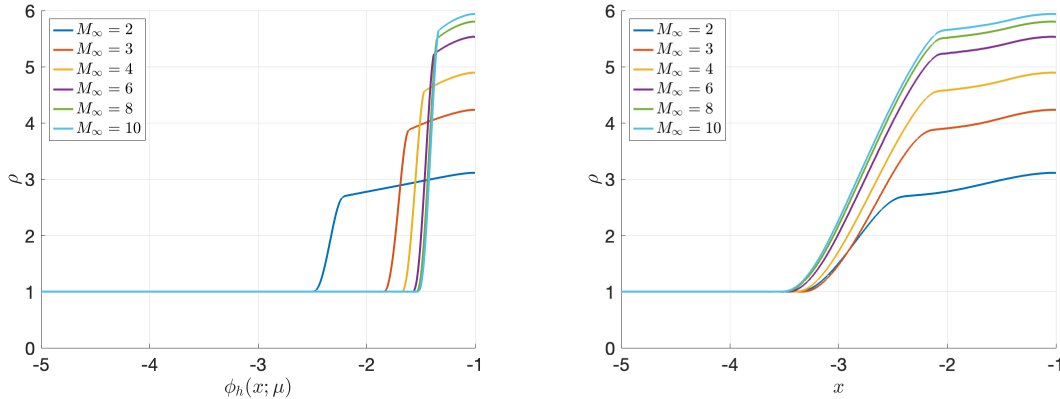


Figure 5: Density along the stagnation line on the adapted meshes \mathcal{T}_h^μ and pulled back to the reference mesh \mathcal{T}_h^0 . The jump in the solution is well-aligned and is spread out over the domain.

For model reduction, the training set is $\mathcal{S}_{\text{train}} = [2, 3, 4, 6, 8, 10]$. We note that the training set is slightly finer for lower Mach numbers. Changing the Mach number moves the shock more in the supersonic regime than in the hypersonic regime, so the parametric problem is actually more challenging on the lower end of the parameter range. Still, this is a relatively coarse training set for the Mach numbers considered.

We see some evidence that the mapped snapshots are more amenable to model reduction in Figure 6 by plotting the decay of the singular values for the snapshots computed on a fixed mesh, \mathbf{u}_h , and those computed on an adapted mesh and pulled back to the reference mesh, $\tilde{\mathbf{u}}_h$. The normalized singular values of the mapped solutions are consistently lower for the solutions mapped back to the reference domain. The difference between the singular value decay is less pronounced than it would be for some other optimal transport-oriented ROMs, as alignment between snapshots is not specifically enforced. Still, the improvement is non-negligible and attained without any extra offline calibration.

The ROMs are tested with a test set $\mathcal{S}_{\text{cyl}} \in \mathcal{D}$ consisting of three equally spaced test parameters between each training parameter, for a total of 15 test points. The accuracy of the RBF ROM for the mappings and solution is shown in Figures 7(a) and 7(b) for different choices of reduced basis size and summarized in Table 1 for $N = 6$. The RBF ROM for the mapping is able to reach below 1% relative error for both x and y components. The RBF ROM shows improvements over the fixed mesh surrogate in terms of average errors on the fixed mesh, with neither surrogate reaching projection error.

The solution profiles themselves, taking into account the mapping, show a dramatic improvement. While the RBF surrogates on the fixed mesh solution are able to achieve reasonable L2 errors for a nonintrusive surrogate, they result in entirely unphysical solutions. On the other hand, the mapped ROM is able to produce solutions that qualitatively match

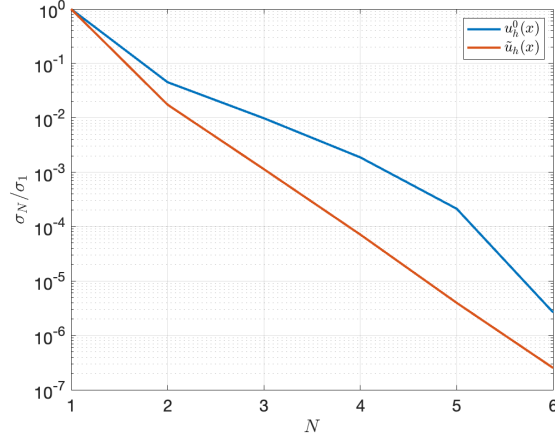


Figure 6: Singular value decay for the cylinder problem comparing fixed mesh solutions to mapped mesh solutions.

| Quantity | Average | Maximum |
|----------------------------|---------|---------|
| $E_{\mathbf{u}_h^0}$ | 0.078 | 0.149 |
| $E_{\tilde{\mathbf{u}}_h}$ | 0.011 | 0.032 |
| E_{ϕ_h} | 0.008 | 0.018 |

Table 1: Mean and max relative errors over $\boldsymbol{\mu} \in \mathcal{S}_{\text{cyl}}$ of fixed mesh ROM for $\mathbf{u}_h^0(\mathbf{x})$ (top row) and mapped mesh ROM for $\tilde{\mathbf{u}}_h(\mathbf{x})$ and $\phi_h(\mathbf{x})$ (bottom two rows) for flow over a cylinder, with no truncation ($N = 6$).

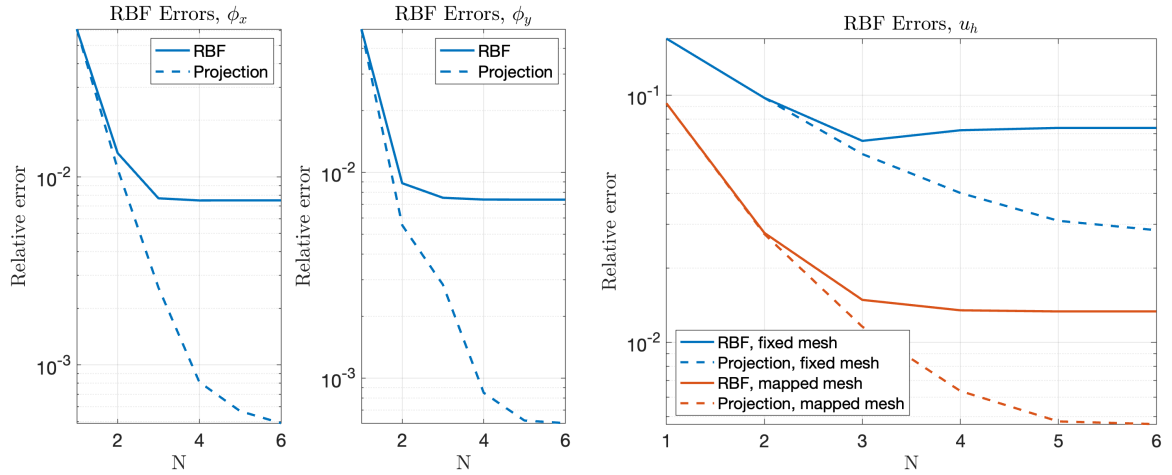


Figure 7: Average RBF ROM relative errors for mesh mapping ϕ_h (left) and solution $\tilde{\mathbf{u}}_h$ (right) for high speed cylinder case.

the true solution, with only some visible differences in the outflow boundaries towards the extremes of the parameter range.

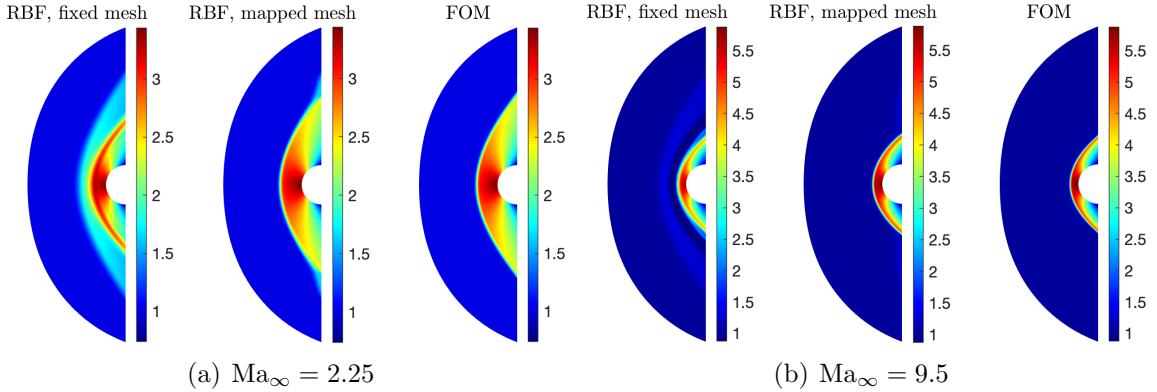


Figure 8: Comparison of fixed mesh and mapped ROMs for parameters with the largest errors in the test set for flow around a cylinder.

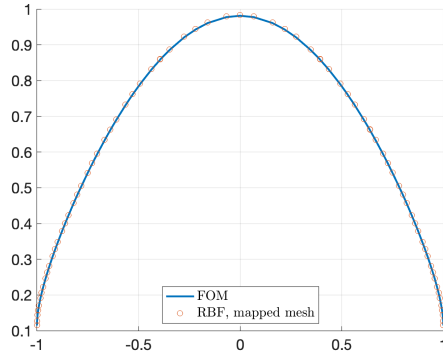


Figure 9: Nondimensionalized wall pressure with FOM and RBF ROM at $Ma_\infty = 2.25$

These irregularities at the outflow are not expected to impact wall quantities; in Figure 9 we can see that wall pressure is indeed captured well by the ROM for the parameter with the largest errors, $\mu = 2.25$.

4.2. Flow over a smooth bump

We repeat the procedure on a flow with more complicated features. This flow over a smooth bump is similar to the problem considered in [30] and is a common benchmark for shock capturing schemes [58, 12, 49]. We consider the case from [58] of supersonic flow over a smooth bump with height 4% in a rectangular domain with length 3 and height 1. Inlet and outlet conditions are set at the left and right boundaries while the top and bottom are inviscid walls. The geometry and initial mesh with 1048 elements is shown in Figure 10(a). We use polynomial order 4 and viscosity continuation for all cases. The Monge-Ampère equation is solved on a rectangular domain and the resulting adapted grid is mapped onto the physical geometry with a simple transformation.

For $Ma_\infty = 1.4$, the solution with and without the adapted mesh is shown in Figures 10(c) and 10(d). The mesh is able to refine towards the initial shocks, the reflections off

of the top wall, and the resulting interactions, leading to sharper shocks throughout the domain.

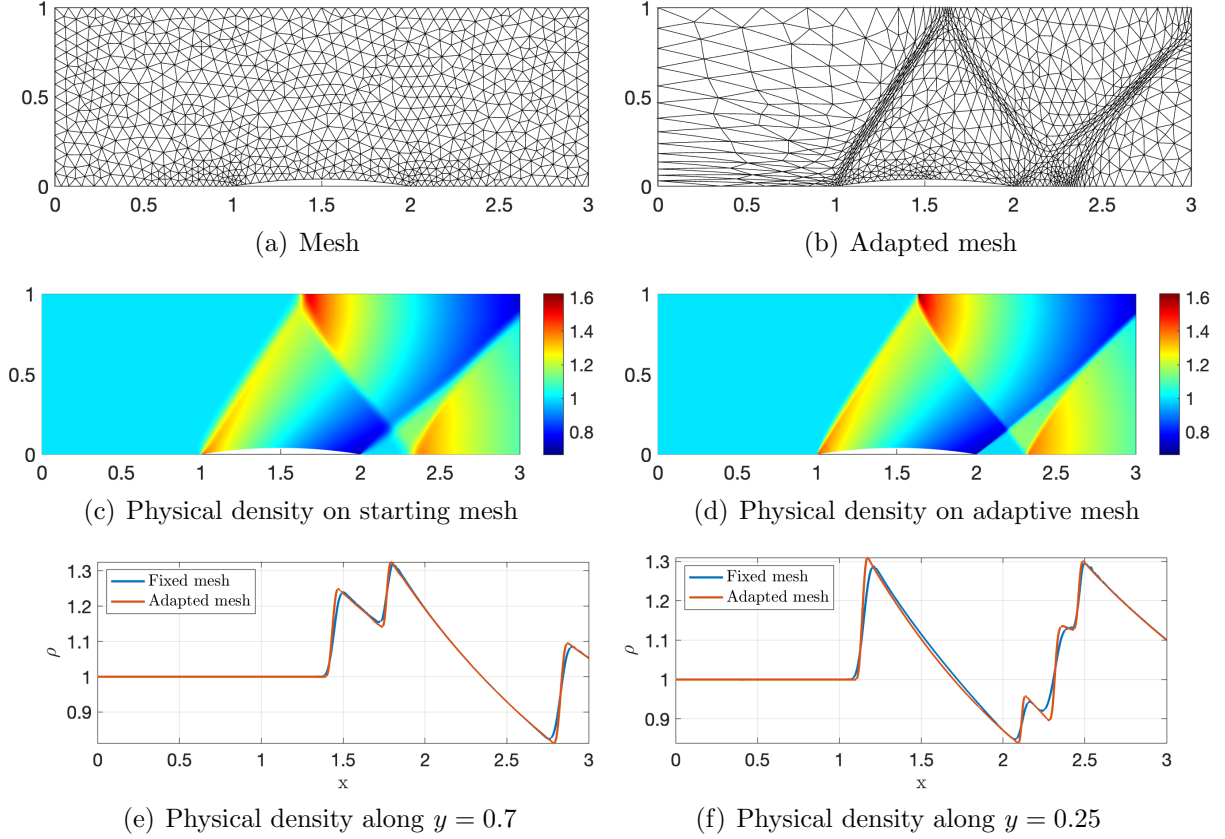


Figure 10: Fixed mesh and adaptive mesh solutions of $\text{Ma}_\infty = 1.4$ flow over the smooth bump.

For the parametric study, we let the Mach number vary from 1.4 to 1.5, which is a smaller parametric variation than in other studies.

We consider two sets of training data of $\mathcal{S}_{\text{train}}^1 = [1.4, 1.45, 1.5]$ and $\mathcal{S}_{\text{train}}^2 = [1.4, 1.425, 1.45, 1.475, 1.5]$. The performance of the ROM is tested at 10 random points in this Mach number range. The average and max errors are given in Table 2. Although there is a consistent reduction in the error, the improvements are much more modest than in the cylinder case. As can be seen in the singular value decay in Figure 11 for $\mathcal{S}_{\text{train}}^1$, the representability of the solution in a linear basis does not change as much as for the cylinder case. Despite this, in Figure 12, we again see that the qualitative nature of the solution is improved with the mapped ROMs. There are fewer noticeable “staircase”-like patterns that are commonly observed in linear model reduction of localized features, although some features are not accurately captured with the sparser training data set.

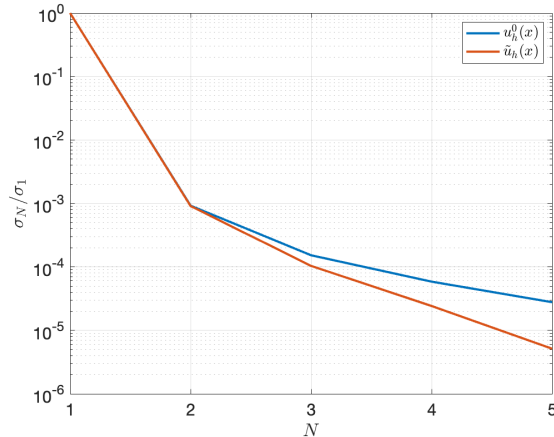


Figure 11: Decay of singular values for bump case with and without mesh mapping for training set $\mathcal{S}_{\text{train}}^2$

| Quantity | Average | Maximum |
|----------------------------|---------|---------|
| $E_{\mathbf{u}_h^0}$ | 0.008 | 0.009 |
| $E_{\tilde{\mathbf{u}}_h}$ | 0.002 | 0.003 |
| E_{ϕ_h} | 0.004 | 0.005 |

Table 2: Mean and max relative errors over $\boldsymbol{\mu} \in \mathcal{S}_{\text{cyl}}$ of fixed mesh ROM for $\mathbf{u}_h^0(\boldsymbol{x})$ (top row) and mapped mesh ROM for $\tilde{\mathbf{u}}_h(\boldsymbol{x})$ and $\phi_h(\boldsymbol{x})$ (bottom two rows) for supersonic flow over a bump. Trained on $\mathcal{S}_{\text{train}}^2$ with no truncation ($N = 5$).

4.3. Double wedge

The final flow setup is taken from [18] and is meant to be an initial step towards double ramp and cone flows. The geometry is a 2D double wedge with angles $\theta_1 = 25^\circ$ and $\theta_2 = 37^\circ$. See Figure 13 for the starting mesh. The bottom wall is assigned an inviscid wall boundary condition, the rightmost wall is assigned an outlet boundary condition, and the other boundaries are treated as supersonic inlets. We use an initial unstructured mesh with 1842 tetrahedral elements with polynomial order 3. The FOM is solved with the viscosity continuation starting from uniform free-stream values.

The ROM is trained on $\mathcal{S}_{\text{train}} = [4, 5, 6, 7]$ and tested at 12 equally spaced Mach numbers between the training set. Visualizations of the FOM and the mesh mapping can be seen in Figure 14. As before, the flow features are brought into closer alignment on Ω and the features are aggressively smoothed out.

We examine the decay of the singular values for the original snapshots and the mapped snapshots to see if this makes the ensemble more amenable to model reduction. Figure 15 shows that the singular values of the mapped solutions are consistently about an order of magnitude smaller than those of the fixed mesh solutions.

The RBF ROM trained on the mapped values is able to produce much more accurate

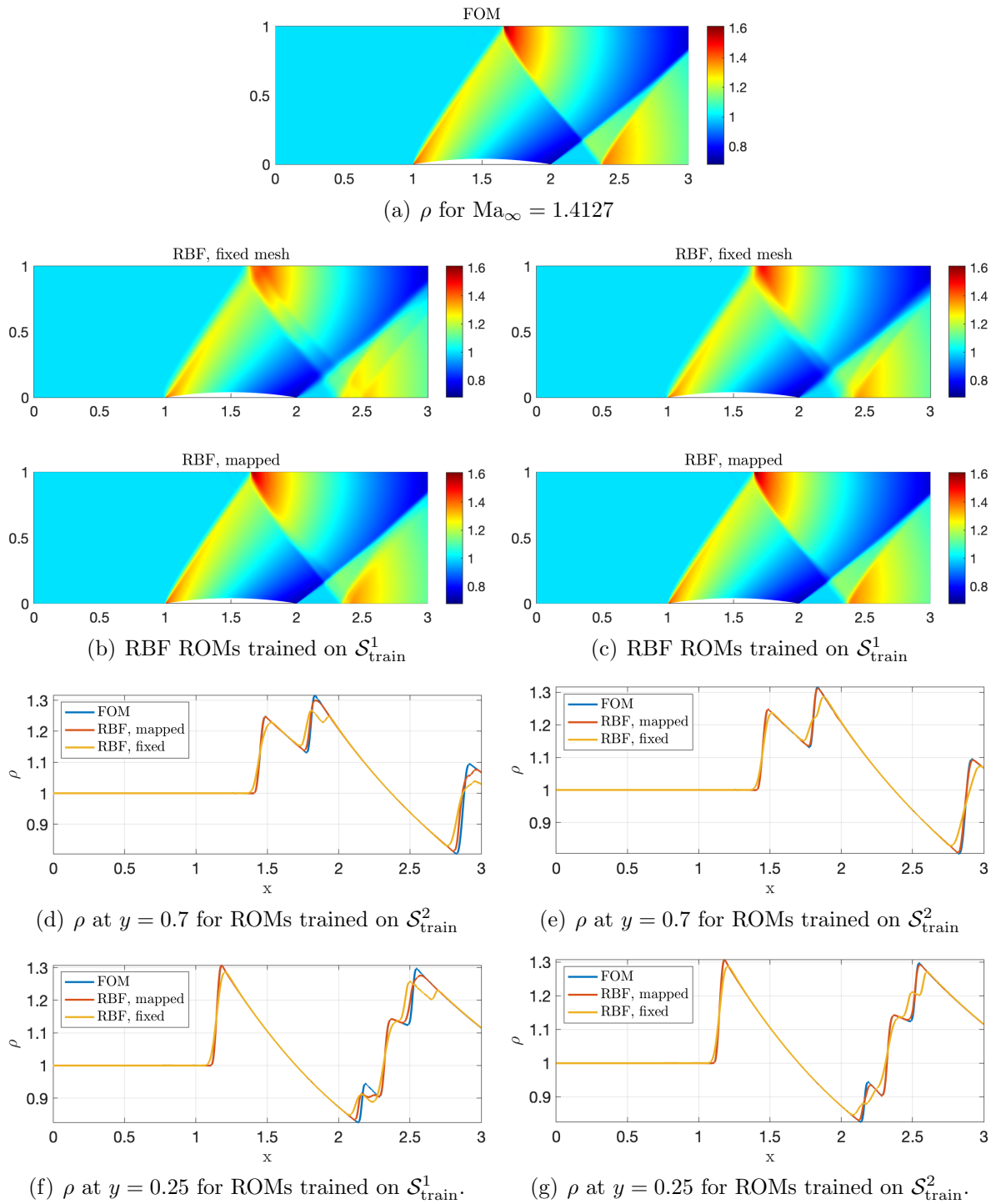


Figure 12: ROM solution profiles for μ with the largest error, trained with different parameter sets.

results, as shown in Table 3. We see in Figure 16 that the average solution errors are substan-

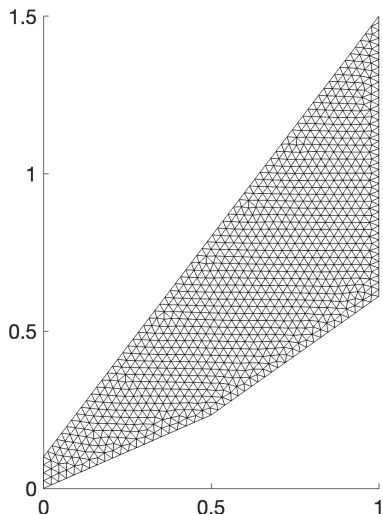


Figure 13: Starting unstructured mesh for double wedge problem

tially smaller for all values of N and that the relative mapping errors are also consistently below 1%. Figure 17 shows again that the RBF ROM with the mesh mapping tends to do a better job producing physically meaningful solutions.

| Quantity | Average | Maximum |
|----------------------------|---------|---------|
| $E_{\mathbf{u}_h^0}$ | 0.061 | 0.116 |
| $E_{\tilde{\mathbf{u}}_h}$ | 0.008 | 0.012 |
| E_{ϕ_h} | 0.002 | 0.003 |

Table 3: Mean and max relative errors over $\boldsymbol{\mu} \in \mathcal{S}_{\text{cyl}}$ of fixed mesh ROM for $\mathbf{u}_h^0(\boldsymbol{x})$ (top row) and mapped mesh ROM for $\tilde{\mathbf{u}}_h(\boldsymbol{x})$ and $\phi_h(\boldsymbol{x})$ (bottom two rows) for hypersonic flow over a double wedge with no truncation ($N = 4$).

5. Conclusions

We have applied an r -adaptive method using high-order solutions of the Monge-Ampère equation to the high-fidelity solution and model reduction of parametrized systems of PDEs with shocks. Using a high-order method for the FOM allows us to iteratively solve and refine on anisotropically adapted, curved grids that track relevant solution features. The usefulness of this approach was then demonstrated on parametrized supersonic and hypersonic flow problems with moving shocks. The approach does not depend on the discretization of the FOM and should work with continuous and discontinuous schemes, as long as they can solve on curved meshes.

Future work includes the application of this method to problems with higher dimensional parameter spaces and more complicated phenomena, such as viscous effects or chemical reactions. The sensor in this work is not designed specifically to track shocks and should

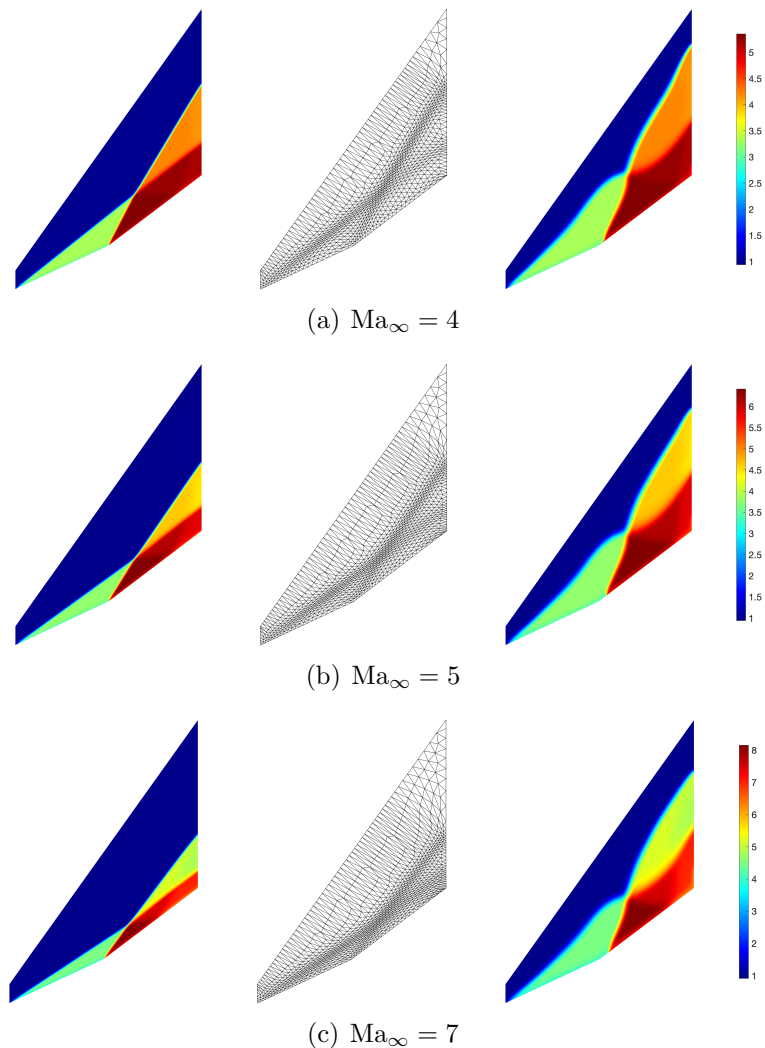


Figure 14: For different Mach numbers, a visualization of the solution $\mathbf{u}_h(\mathbf{x})$, the corresponding adapted mesh \mathcal{T}_h^μ and the solution mapped back to the reference mesh $\tilde{\mathbf{u}}_h$. Plotted quantity is density.

be able to refine towards other features. One challenge is that for viscous problems useful targets for refinement of the FOM, such as a boundary layer, may not be the features that need to be tracked in a model reduction process.

In order to apply the Monge-Ampère equation to more challenging problems, its efficiency needs to be addressed. The Newton method from [60] should be more efficient than the fixed point method used here, but it requires the linearization of the solution-dependent sensor. Another target for efficiency gains is the evaluation of the sensor itself during the solution process, which is now handled with high-order interpolation. A more efficient approach would be to evaluate the sensor on a fine structured grid allowing for more rapid interpolation, as is done with the sensors in [40].

More study is needed for the solution of the Monge-Ampère equation on non-convex

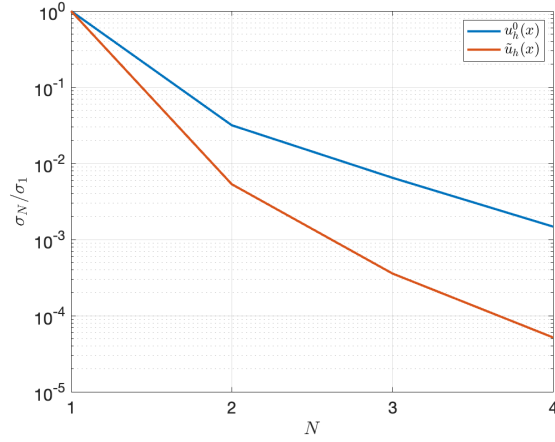


Figure 15: Decay of singular values for double wedge case with and without mesh mapping

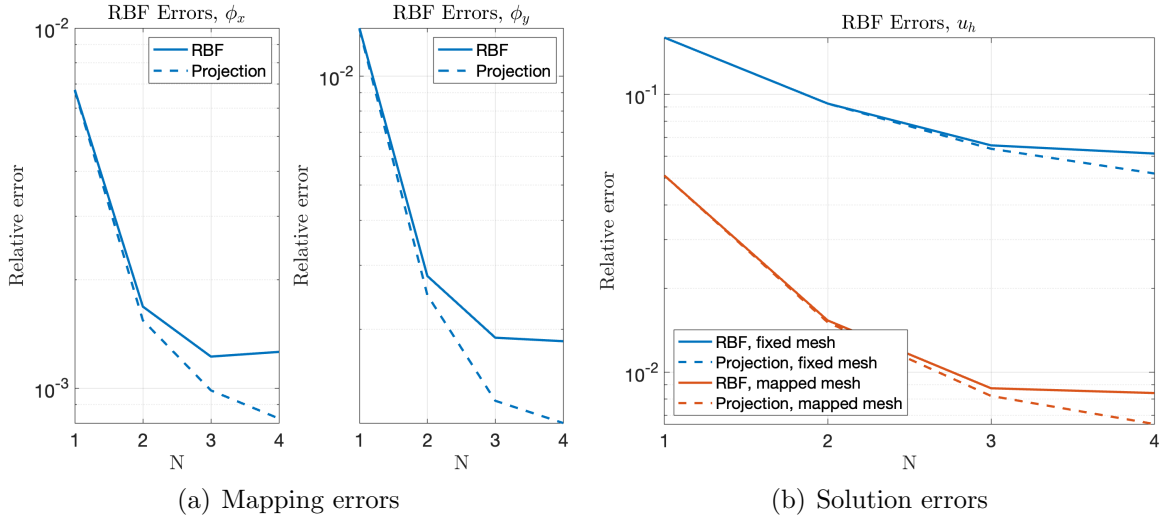


Figure 16: RBF ROM relative errors for mesh mapping ϕ_h and solution \tilde{u}_h

domains and domains with corners. In these cases, it might be preferable to use different PDEs for r -adaptivity such as a variational approach that directly controls node locations and element quality [32]. While the Monge-Ampère equation is an effective method for mesh adaptivity with good guarantees on mesh quality, the described model reduction approach will work for any PDE-based r -adaptivity method.

Finally, this approach can be coupled with intrusive ROMs and automated sampling procedures for greater accuracy and more robust performance when extrapolating.

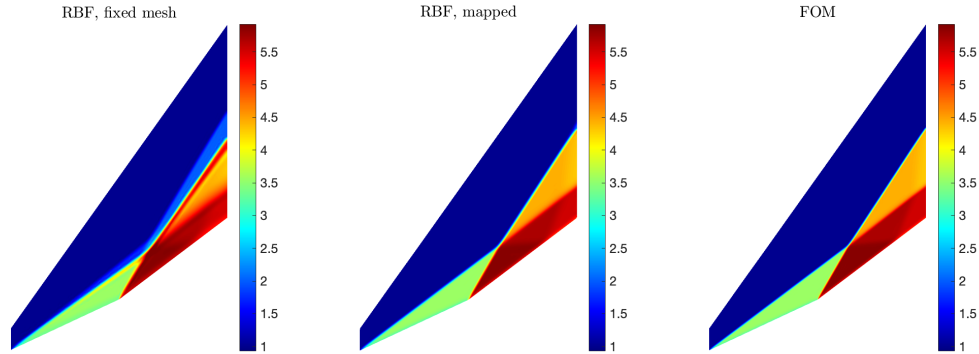


Figure 17: Comparison of the fixed mesh and mapped mesh ROMs for $Ma_\infty = 4.5$

Acknowledgements

We gratefully acknowledge the United States Department of Energy under contract DE-NA0003965.

This article has been authored by an employee of National Technology & Engineering Solutions of Sandia, LLC under Contract No. DE-NA0003525 with the U.S. Department of Energy (DOE). The employee owns all right, title and interest in and to the article and is solely responsible for its contents. The United States Government retains and the publisher, by accepting the article for publication, acknowledges that the United States Government retains a non-exclusive, paid-up, irrevocable, world-wide license to publish or reproduce the published form of this article or allow others to do so, for United States Government purposes. The DOE will provide public access to these results of federally sponsored research in accordance with the DOE Public Access Plan <https://www.energy.gov/downloads/doe-public-access-plan>. SAND2023-102770.

References

- [1] Yifan Bai and Krzysztof J Fidkowski. Continuous artificial-viscosity shock capturing for hybrid discontinuous galerkin on adapted meshes. *AIAA Journal*, 60(10):5678–5691, 2022.
- [2] Joshua Barnett and Charbel Farhat. Quadratic approximation manifold for mitigating the kolmogorov barrier in nonlinear projection-based model order reduction. *Journal of Computational Physics*, 464:111348, 2022.
- [3] Joshua Barnett, Charbel Farhat, and Yvon Maday. Neural-network-augmented projection-based model order reduction for mitigating the kolmogorov barrier to reducibility. *Journal of Computational Physics*, page 112420, 2023.
- [4] Nicolas Barral, Tommaso Taddei, and Ishak Tifouti. Registration-based model reduction of parameterized pdes with spatio-parameter adaptivity. *arXiv preprint arXiv:2308.01773*, 2023.
- [5] Garrett E Barter and David L Darmofal. Shock capturing with pde-based artificial viscosity for dgfm: Part i. formulation. *Journal of Computational Physics*, 229(5):1810–1827, 2010.
- [6] Tobias Blickhan. A registration method for reduced basis problems using linear optimal transport. *arXiv preprint arXiv:2304.14884*, 2023.

- [7] Patrick J Blonigan, Francesco Rizzi, Micah Howard, Jeffrey A Fike, and Kevin T Carlberg. Model reduction for steady hypersonic aerodynamics via conservative manifold least-squares petrov–galerkin projection. *AIAA Journal*, 59(4):1296–1312, 2021.
- [8] Yann Brenier. Polar factorization and monotone rearrangement of vector-valued functions. *Communications on pure and applied mathematics*, 44(4):375–417, 1991.
- [9] Chris J Budd, Weizhang Huang, and Robert D Russell. Adaptivity with moving grids. *Acta Numerica*, 18:111–241, 2009.
- [10] Chris J Budd, Andrew TT McRae, and Colin J Cotter. The scaling and skewness of optimally transported meshes on the sphere. *Journal of Computational Physics*, 375:540–564, 2018.
- [11] CJ Budd and E Walsh. The geometry of r-adaptive meshes generated using optimal transport methods. *Journal of Computational Physics*, 282:113–137, 2015.
- [12] Anne Burbeau, Pierre Sagaut, and Ch-H Bruneau. A problem-independent limiter for high-order runge–kutta discontinuous galerkin methods. *Journal of Computational Physics*, 169(1):111–150, 2001.
- [13] Luis A Caffarelli. Interior w_2, p estimates for solutions of the monge-ampere equation. *Annals of Mathematics*, pages 135–150, 1990.
- [14] Nicolas Cagniard, Yvon Maday, and Benjamin Stamm. Model order reduction for problems with large convection effects. *Contributions to partial differential equations and applications*, pages 131–150, 2019.
- [15] Graham Candler, Michael Barnhardt, Travis Drayna, Ioannis Nompelis, David Peterson, and Pramod Subbareddy. Unstructured grid approaches for accurate aeroheating simulations. In *18th AIAA computational fluid dynamics conference*, page 3959, 2007.
- [16] Graham V Candler, Heath B Johnson, Ioannis Nompelis, Vladimir M Gidzak, Pramod K Subbareddy, and Michael Barnhardt. Development of the us3d code for advanced compressible and reacting flow simulations. In *53rd AIAA Aerospace Sciences Meeting*, page 1893, 2015.
- [17] Kevin Carlberg. Adaptive h-refinement for reduced-order models. *International Journal for Numerical Methods in Engineering*, 102(5):1192–1210, 2015.
- [18] Brian Carnes, V Gregory Weirs, and Thomas Smith. Code verification and numerical error estimation for use in model validation of laminar, hypersonic double-cone flows. In *AIAA Scitech 2019 Forum*, page 2175, 2019.
- [19] David S Ching, Patrick J Blonigan, Francesco Rizzi, and Jeffrey A Fike. Reduced order modeling of hypersonic aerodynamics with grid tailoring. In *AIAA SCITECH 2022 Forum*, page 1247, 2022.
- [20] Eric J Ching, Andrew D Kercher, and Andrew T Corrigan. The moving discontinuous galerkin method with interface condition enforcement for robust simulations of high-speed viscous flows. In *AIAA SCITECH 2023 Forum*, page 1975, 2023.
- [21] Eric J Ching, Yu Lv, Peter Gnoffo, Michael Barnhardt, and Matthias Ihme. Shock capturing for discontinuous galerkin methods with application to predicting heat transfer in hypersonic flows. *Journal of Computational Physics*, 376:54–75, 2019.
- [22] Bernardo Cockburn and Chi-Wang Shu. Tvb runge-kutta local projection discontinuous galerkin finite element method for conservation laws. ii. general framework. *Mathematics of computation*, 52(186):411–435, 1989.
- [23] Andrew Corrigan, Andrew D Kercher, and David A Kessler. A moving discontinuous galerkin finite element method for flows with interfaces. *International Journal for Numerical Methods in Fluids*, 89(9):362–406, 2019.
- [24] Andrea F Cortesi, Paul G Constantine, Thierry E Magin, and Pietro M Congedo. Forward and backward uncertainty quantification with active subspaces: application to hypersonic flows around a cylinder. *Journal of Computational Physics*, 407:109079, 2020.
- [25] Kelsey L DiPietro and Alan E Lindsay. Adaptive solution to two-dimensional partial differential equations in curved domains using the monge–ampere equation. *SIAM Journal on Scientific Computing*, 41(2):A1331–A1356, 2019.
- [26] Valentina Dolci, Renzo Arina, et al. Proper orthogonal decomposition as surrogate model for aerodynamic optimization. *International Journal of Aerospace Engineering*, 2016, 2016.
- [27] P. Fernandez, A. Christophe, S. Terrana, N. C. Nguyen, and J. Peraire. Hybridized discontinuous

- Galerkin methods for wave propagation. *Journal of Scientific Computing*, 77(3):1566–1604, dec 2018.
- [28] P. Fernandez, N. C. Nguyen, and J. Peraire. The hybridized Discontinuous Galerkin method for Implicit Large-Eddy Simulation of transitional turbulent flows. *Journal of Computational Physics*, 336:308–329, 2017.
- [29] Pablo Fernandez, Cuong Nguyen, and Jaime Peraire. A physics-based shock capturing method for unsteady laminar and turbulent flows. In *2018 AIAA Aerospace Sciences Meeting*, page 0062, 2018.
- [30] Andrea Ferrero, Tommaso Taddei, and Lei Zhang. Registration-based model reduction of parameterized two-dimensional conservation laws. *Journal of Computational Physics*, 457:111068, 2022.
- [31] K. J. Fidkowski. A hybridized discontinuous Galerkin method on mapped deforming domains. *Computers and Fluids*, 139:80–91, 2016.
- [32] Meire Fortunato and Per-Olof Persson. High-order unstructured curved mesh generation using the Winslow equations. *Journal of Computational Physics*, 307:1–14, 2016.
- [33] Sokratia Georgaka, Giovanni Stabile, Kelbij Star, Gianluigi Rozza, and Michael J Bluck. A hybrid reduced order method for modelling turbulent heat transfer problems. *Computers & Fluids*, 208:104615, 2020.
- [34] Shijin Hou, Yanlai Chen, and Yinhua Xia. Fast l^2 optimal mass transport via reduced basis methods for the Monge–Ampère equation. *SIAM Journal on Scientific Computing*, 44(6):A3536–A3559, 2022.
- [35] Micah Howard, Andrew Bradley, Steven W Bova, James Overfelt, Ross Wagnild, Derek Dinzl, Mark Hoemmen, and Alicia Klinvex. Towards performance portability in a compressible CFD code. In *23rd AIAA Computational Fluid Dynamics Conference*, page 4407, 2017.
- [36] Cheng Huang and Karthik Duraisamy. Predictive reduced order modeling of chaotic multi-scale problems using adaptively sampled projections. *arXiv preprint arXiv:2301.09006*, 2023.
- [37] Tianci Huang and Matthew J Zahr. A robust, high-order implicit shock tracking method for simulation of complex, high-speed flows. *Journal of Computational Physics*, 454:110981, 2022.
- [38] Antonio Huerta, E Casoni, and Jaime Peraire. A simple shock-capturing technique for high-order discontinuous galerkin methods. *International journal for numerical methods in fluids*, 69(10):1614–1632, 2012.
- [39] Angelo Iollo and Damiano Lombardi. Advection modes by optimal mass transfer. *Physical Review E*, 89(2):022923, 2014.
- [40] Angelo Iollo and Tommaso Taddei. Mapping of coherent structures in parameterized flows by learning optimal transportation with gaussian models. *Journal of Computational Physics*, 471:111671, 2022.
- [41] Youngkyu Kim, Youngsoo Choi, David Widemann, and Tarek Zohdi. A fast and accurate physics-informed neural network reduced order model with shallow masked autoencoder. *Journal of Computational Physics*, 451:110841, 2022.
- [42] Lilia Krivodonova. Limiters for high-order discontinuous galerkin methods. *Journal of Computational Physics*, 226(1):879–896, 2007.
- [43] Lilia Krivodonova, Jianguo Xin, J-F Remacle, Nicolas Chevaugeon, and Joseph E Flaherty. Shock detection and limiting with discontinuous galerkin methods for hyperbolic conservation laws. *Applied Numerical Mathematics*, 48(3-4):323–338, 2004.
- [44] Zubin J Lal, Graham V Candler, and Bernardo J Cockburn. Aeroheating predictions of hypersonic flight geometries with high-order discontinuous galerkin methods. In *AIAA SCITECH 2023 Forum*, page 0854, 2023.
- [45] Kookjin Lee and Kevin T Carlberg. Model reduction of dynamical systems on nonlinear manifolds using deep convolutional autoencoders. *Journal of Computational Physics*, 404:108973, 2020.
- [46] Patrick LeGresley and Juan Alonso. Dynamic domain decomposition and error correction for reduced order models. In *41st Aerospace Sciences Meeting and Exhibit*, page 250, 2003.
- [47] Clayton Little and Charbel Farhat. Nonlinear projection-based model order reduction in the presence of adaptive mesh refinement. In *AIAA SCITECH 2023 Forum*, page 2682, 2023.
- [48] Yu Lv and Matthias Ihme. Entropy-bounded discontinuous galerkin scheme for Euler equations. *Journal of Computational Physics*, 295:715–739, 2015.
- [49] John Francis Lynn. *Multigrid solution of the Euler equations with local preconditioning*. University of

- Michigan, 1995.
- [50] Robert W MacCormack. Carbuncle computational fluid dynamics problem for blunt-body flows. *Journal of Aerospace Information Systems*, 10(5):229–239, 2013.
 - [51] Georg May, Koen Devesse, Ajay Rangarajan, and Thierry Magin. A hybridized discontinuous galerkin solver for high-speed compressible flow. *Aerospace*, 8(11):322, 2021.
 - [52] Andrew TT McRae, Colin J Cotter, and Chris J Budd. Optimal-transport-based mesh adaptivity on the plane and sphere using finite elements. *SIAM Journal on Scientific Computing*, 40(2):A1121–A1148, 2018.
 - [53] Marzieh Alireza Mirhoseini and Matthew J Zahr. Model reduction of convection-dominated partial differential equations via optimization-based implicit feature tracking. *arXiv preprint arXiv:2109.14694*, 2021.
 - [54] Marzieh Alireza Mirhoseini and Matthew J Zahr. Accelerated solutions of convection-dominated partial differential equations using implicit feature tracking and empirical quadrature. *arXiv preprint arXiv:2305.15661*, 2023.
 - [55] D. Moro, N. C. Nguyen, and J. Peraire. Navier-stokes solution using Hybridizable discontinuous Galerkin methods. In *20th AIAA Computational Fluid Dynamics Conference 2011*, pages AIAA–2011–3407, Honolulu, Hawaii, jun 2011. American Institute of Aeronautics and Astronautics.
 - [56] David Moro, Ngoc Cuong Nguyen, and Jaime Peraire. Dilation-based shock capturing for high-order methods. *International Journal for Numerical Methods in Fluids*, 82(7):398–416, 2016.
 - [57] Nirmal J Nair and Maciej Balajewicz. Transported snapshot model order reduction approach for parametric, steady-state fluid flows containing parameter-dependent shocks. *International Journal for Numerical Methods in Engineering*, 117(12):1234–1262, 2019.
 - [58] Cuong Nguyen and Jaime Peraire. An adaptive shock-capturing hdg method for compressible flows. In *20th AIAA Computational Fluid Dynamics Conference*, page 3060, 2011.
 - [59] N. C. Nguyen and J. Peraire. Hybridizable discontinuous Galerkin methods for partial differential equations in continuum mechanics. *Journal of Computational Physics*, 231(18):5955–5988, jul 2012.
 - [60] Ngoc Cuong Nguyen and Jaime Peraire. Hybridizable discontinuous galerkin methods for the monge-ampere equation. *arXiv preprint arXiv:2306.05296*, 2023.
 - [61] Ngoc Cuong Nguyen, Jordi Vila-Perez, and Jaime Peraire. An adaptive viscosity regularization approach for the numerical solution of conservation laws: Application to finite element methods. *arXiv preprint arXiv:2305.00461*, 2023.
 - [62] Benjamin Peherstorfer. Model reduction for transport-dominated problems via online adaptive bases and adaptive sampling. *SIAM Journal on Scientific Computing*, 42(5):A2803–A2836, 2020.
 - [63] J. Peraire, N. C. Nguyen, and B. Cockburn. A hybridizable discontinuous Galerkin method for the compressible euler and Navier-Stokes equations. In *48th AIAA Aerospace Sciences Meeting Including the New Horizons Forum and Aerospace Exposition*, pages AIAA 2010–363, 2010.
 - [64] Per-Olof Persson. Shock capturing for high-order discontinuous galerkin simulation of transient flow problems. In *21st AIAA computational fluid dynamics conference*, page 3061, 2013.
 - [65] Per-Olof Persson and Jaime Peraire. Sub-cell shock capturing for discontinuous galerkin methods. In *44th AIAA Aerospace Sciences Meeting and Exhibit*, page 112, 2006.
 - [66] Per-Olof Persson and Benjamin Stamm. A discontinuous galerkin method for shock capturing using a mixed high-order and sub-grid low-order approximation space. *Journal of Computational Physics*, 449:110765, 2022.
 - [67] Raaghav Ramani and Steve Shkoller. A fast dynamic smooth adaptive meshing scheme with applications to compressible flow. *Journal of Computational Physics*, page 112280, 2023.
 - [68] Jaideep Ray, Patrick Blonigan, Eric T Phipps, and Kathryn Maupin. An assessment of the laminar hypersonic double-cone experiments in the lens-xx tunnel. *AIAA Journal*, 61(8):3298–3312, 2023.
 - [69] Francesco Romor, Giovanni Stabile, and Gianluigi Rozza. Non-linear manifold reduced-order models with convolutional autoencoders and reduced over-collocation method. *Journal of Scientific Computing*, 94(3):74, 2023.
 - [70] Kevin M Sabo, Benjamin L Couchman, Wesley L Harris, and David L Darmofal. Investigation of

- thermochemical non-equilibrium models in hypersonic flows using output-based mesh adaptation. In *AIAA SCITECH 2022 Forum*, page 0343, 2022.
- [71] David Saunders, Seokkwan Yoon, and Michael Wright. An approach to shock envelope grid tailoring and its effect on reentry vehicle solutions. In *45th AIAA Aerospace Sciences Meeting and Exhibit*, page 207, 2007.
 - [72] Michael K Sleeman and Masayuki Yano. Goal-oriented model reduction for parametrized time-dependent nonlinear partial differential equations. *Computer Methods in Applied Mechanics and Engineering*, 388:114206, 2022.
 - [73] Matthias Sonntag and Claus-Dieter Munz. Efficient parallelization of a shock capturing for discontinuous galerkin methods using finite volume sub-cells. *Journal of Scientific Computing*, 70:1262–1289, 2017.
 - [74] Tommaso Taddei. A registration method for model order reduction: data compression and geometry reduction. *SIAM Journal on Scientific Computing*, 42(2):A997–A1027, 2020.
 - [75] Sergio Torregrosa, Victor Champaney, Amine Ammar, Vincent Herbert, and Francisco Chinesta. Surrogate parametric metamodel based on optimal transport. *Mathematics and Computers in Simulation*, 194:36–63, 2022.
 - [76] Julie Tryoen, Pietro Marco Congedo, Remi Abgrall, N Villedieu, and TE Magin. Bayesian-based method with metamodels for rebuilding freestream conditions in atmospheric entry flows. *AIAA Journal*, 52(10):2190–2197, 2014.
 - [77] Jordi Vila-Pérez, Matteo Giacomini, and Antonio Huerta. Benchmarking the face-centred finite volume method for compressible laminar flows. *International Journal of Numerical Methods for Heat & Fluid Flow*, 33(6):2198–2231, 2023.
 - [78] Jordi Vila-Pérez, Matteo Giacomini, Ruben Sevilla, and Antonio Huerta. Hybridisable Discontinuous Galerkin Formulation of Compressible Flows. *Archives of Computational Methods in Engineering*, 28(2):753–784, 2021.
 - [79] Dunhui Xiao, Fangxin Fang, Christopher Pain, and Guangwei Hu. Non-intrusive reduced-order modelling of the navier–stokes equations based on rbf interpolation. *International Journal for Numerical Methods in Fluids*, 79(11):580–595, 2015.
 - [80] Masayuki Yano, James Modisette, and David Darmofal. The importance of mesh adaptation for higher-order discretizations of aerodynamic flows. In *20th AIAA Computational Fluid Dynamics Conference*, page 3852, 2019.
 - [81] Matthew J Zahr and Joseph M Powers. High-order resolution of multidimensional compressible reactive flow using implicit shock tracking. *AIAA Journal*, 59(1):150–164, 2021.
 - [82] Matthew J Zahr, Andrew Shi, and P-O Persson. Implicit shock tracking using an optimization-based high-order discontinuous galerkin method. *Journal of Computational Physics*, 410:109385, 2020.
 - [83] Victor Zucatti and Matthew J Zahr. An adaptive, training-free reduced-order model for convection-dominated problems based on hybrid snapshots. *arXiv preprint arXiv:2301.01718*, 2023.